International Journal of Thermal Sciences 157 (2020) 106503

Contents lists available at ScienceDirect

International Journal of Thermal Sciences

journal homepage: http://www.elsevier.com/locate/ijts

Free convection heat transfer analysis of a suspension of nano–encapsulated phase change materials (NEPCMs) in an inclined porous cavity

Mohammad Ghalambaz [a,b], S.A.M. Mehryan [c], Iman Zahmatkesh [d], Ali Chamkha [e,f,*]

[a] Metamaterials for Mechanical, Biomechanical and Multiphysical Applications Research Group, Ton Duc Thang University, Ho Chi Minh City, Vietnam
[b] Faculty of Applied Sciences, Ton Duc Thang University, Ho Chi Minh City, Vietnam
[c] Young Researchers and Elite Club, Yasooj Branch, Islamic Azad University, Yasooj, Iran
[d] Department of Mechanical Engineering, Mashhad Branch, Islamic Azad University, Mashhad, Iran
[e] Institute of Research and Development, Duy Tan University, Da Nang, 550000, Vietnam
[f] Institute of Theoretical and Applied Research (ITAR), Duy Tan University, Hanoi, 100000, Vietnam

ARTICLE INFO

Keywords:
Nano–encapsulated phase change materials (NEPCMs)
Porous media
Cavity
Free convection
Fusion temperature
Stefan number

ABSTRACT

In the current study, free convection heat transfer of a suspension of Nano–Encapsulated Phase Change Materials (NEPCMs) is simulated and discussed in an inclined porous cavity. The phase change materials are capsulated in nano-shells layers, while the core stores/releases large amounts of energy during melting/solidification in the vicinity of the hot/cold walls. The governing equations are introduced and transformed into non–dimensional form before being solved by using the finite element method. Simulation results are validated thoroughly. Thereafter, the consequences of the fusion temperature and the Stefan number on the distributions of streamlines, isotherms, and the heat capacity ratio, as well as the heat transfer characteristics, are analyzed for different inclination angles of the cavity. Inspection of the results demonstrates that the best heat transfer performance occurs for the non–dimensional fusion temperature of 0.5 and the inclination angle of 42°. It is found that a decrease in the Stefan number improves heat transfer. The results also show that the presence of the NEPCM particles generally leads to heat transfer improvement.

1. Introduction

In the recent decade, heat transfer augmentation through using nanofluid–saturated porous media has been a hot topic among scientists. This occurs since nanofluids, which are suspensions of host fluid and high thermal conductivity solid nanoparticles, show better thermal behaviour than regular fluids. On the other hand, a porous medium provides a large fluid-solid contact area as well as an erratic motion of the fluid through the pores which elevate the heat transfer. Mahdi et al. [1], Kasaeian et al. [2], and Menni et al. [3] have provided excellent reviews of nanofluids transport in porous media. These reviews indicate that free convection heat transfer of nanofluids in porous cavities has gained extensive attention because of the relation to the thermal performance of many engineering installations. Some recent works on the subject are the studies of Alsabery et al. [4], Mehryan et al. [5], Chamkha et al. [6], and Zahmatkesh and Habibi [7]. The natural convection heat transfer of various nanofluids, such as carbon nanotubes-water [8], alumina-water [9,10], Ag-water, and titania water [11] has been addressed in the literature.

Recently, the suspension of Nano–Encapsulated Phase Change Materials (NEPCMs) has been introduced as an innovative kind of nanofluids. In such a suspension, Phase Change Materials (PCMs) are enclosed in nano-shells to prevent leakage. In this configuration, the core layer, including a PCM, can store/release large amounts of energy during melting/solidification at a specific fusion temperature.

Different kinds of NEPCM particles have been synthesized. For instance, Zhu et al. [12] encapsulated n–octadecane within SiO_2/graphene composite shells. Meanwhile, Shi et al. [13] prepared nanocapsules with paraffin as the core and polymethyl methacrylate (PMMA) as the shell. Excellent reviews of encapsulation technologies for solid-liquid phase change materials have been provided by Jamekhorshidet al. [14], Su et al. [15], and Liu et al. [16].

The nano–encapsulated phase change materials need to be distinguished from nano-enhanced phase change materials, although both have been abbreviated as NEPCMs. In a nano-enhanced phase change

* Corresponding author.
E-mail addresses: mohammad.ghalambaz@tdtu.edu.vn (M. Ghalambaz), alal171366244@gmail.com (S.A.M. Mehryan), Zahmatkesh5310@mshdiau.ac.ir (I. Zahmatkesh), alichamkha@duytan.edu.vn (A. Chamkha).

https://doi.org/10.1016/j.ijthermalsci.2020.106503
Received 15 September 2019; Received in revised form 22 May 2020; Accepted 23 May 2020
Available online 8 June 2020

Nomenclature

a	Indicator of the position of hot element
b	Indicator of the position of cold element
C	Constant pressure specific heat ($Jkg^{-1}K^{-1}$)
Cr	The heat capacity ratio (suspension/base fluid)
g	Gravity constant (ms^{-2})
l	Length of the thermal elements
H	Size of the cavity, the characteristic length
k	Coefficient of the thermal conductivity ($Wm^{-1}K^{-1}$)
Nc	The number of thermal conductivity for the suspension
Nu	Nusselt number
Nv	The number of dynamic viscosity for the suspension
p	Dimensional pressure (Pa)
P	Dimensionless pressure
Pr	Prandtl number
Ra	Rayleigh number
Ste	Stefan number
T	Dimensional temperature field (K)
TMr	Dimensional melting range (K)
u, U	Dimensional (ms^{-1}) and non-dimensional x-velocity component
v, V	Dimensional (ms^{-1}) and non-dimensional y-velocity component
x, X	Dimensional (m) and non-dimensional x-Cartesian coordinate
y, Y	Dimensional (m) and non-dimensional y-Cartesian coordinate

Greek symbols

μ	Dynamic viscosity ($kgs^{-1}m^{-1}$)
α	Coefficient of thermal diffusivity (m^2s^{-1})
β	Coefficient of thermal expansion (K^{-1})
γ	Inclination angle of the cavity
δ	Non-dimensional phase change band
ε	Porosity
θ	Temperature field in a non-dimensional form
ι	Core-shell weight ratio
λ	Heat capacity ratio
χ	Weight ratio of the core/shell for NEPCM particle
ρ	Density (kgm^{-3})
σ	Non-dimensional fusion function
φ	Volumetric fraction of the encapsulated particles in the host fluid
ψ	Stream-function

Subscript

b	Bulk properties
c	The core of NEPCM particle, Cold wall
f	Pure fluid
h	Hot surface
l	Local value
p	NEPCM particles
s	Porous matrix
sh	Shell of NEPCM particle

material, solid nanoparticles are adding to a PCM to improve its thermal behaviour. Bondareva et al. [17], Hosseinzadeh et al. [18], Singh et al. [19], and Martín et al. [20] have contributed with some significant findings in this field. A comprehensive review of thermophysical properties, applications, and challenges of nano-enhanced phase change materials was given by Leong et al. [21].

The suspension of NEPMCs as working fluid is promising for maintaining sensitive devices such as detectors, computer chipsets, and laser optical alignment systems within a certain temperature range to avoid internal thermal stress. Several authors tried to use NEPCM particles for heat transfer improvements in the forced convection regime. Some recent works are as follows:

Wu et al. [22] experimentally dispersed nano–encapsulated indium within bare or silica shells into poly–α–olefin (PAO) flowing through a microchannel heat exchanger. Both of the NEPCM particles led to almost the same heat transfer performance, which was higher than that of the pure PAO. Seyf et al. [23] neglected the effect of the shell layer and developed a mathematical model for the flow of octadecane NEPCM particles dispersed into PAO through a microtube heat sink. Significant improvement in heat transfer at the cost of tremendous pressure drop was observed due to the addition of the NEPCM particles. This effect was further reported in the investigations of Rehman et al. [24] and Joseph and Sajith [25]. Rehman et al. [24] performed a numerical study for jet impingement of n–octadecane NEPCM particles dispersed into the water while Joseph and Sajith [25] experimentally investigated the flow of polystyrene encapsulated n–octadecane NEPCM particles dispersed into deionized water through square channels.

Rajabifar et al. [26] used NEPCM slurry for cooling of a micro pin fin heat sink. The Nusselt number was observed to be enhanced when utilizing the NEPCM slurry as an advanced coolant. Also, it was found that the Euler number is increasingly affected by the volume fraction of the NEPCMs particles, and intensifies with decreasing the initial velocity. The impact of adding the NEPCM particles to the base fluid on the forced convection heat transfer of a laminar flow passing a solid cylinder was studied by Seyf et al. [27]. The results showed that the slurry flow remarkably enhances the heat transfer compared to the case of pure fluid. Also, it was found that the melting temperature window of the core of NEPCM particles slightly affects the heat transfer. Lu et al. [28] analyzed the heat transfer characteristics of slurry flow in a backwards-facing step channel. The heat transfer coefficient was improved up to 67% by utilizing a slurry as working fluid compared to the water. Meanwhile, Kharati-koopaee and Ghaedi [29] discussed how the step height and the particle diameter might change flow and heat transfer of water-NEPCM over a backwards-facing step. Recently, Ghalambaz et al. [30] discussed mixed convection boundary layer flow and heat transfer over a vertical plate embedded in a porous medium filled with a suspension of polyurethane encapsulated nonadecane NEPCM particles dispersed into water. They found that reduction in the fusion temperature of NEPCMs improves the heat transfer.

Although such developments are important, the thermal behaviour of NEPCMs suspensions in the free convection regime has not been fully understood. The only available work goes back to the study of Ghalambaz et al. [31]. They simulated free convection heat transfer of nano–encapsulated n–octadecane within PMMA shells dispersed into the water in a cavity. Their results demonstrated that an optimum range exists for the non–dimensional fusion temperature to achieve the best heat transfer performance. They also indicated that there is a direct relationship between the latent heat of the NEPCMs cores and the heat transfer rate.

The above literature survey indicates that there is plenty of room to study natural convection of nanofluids containing NEPCM particles in porous filled enclosures. In free convective flows, gravity is a key influencing factor while its consequences may be even higher in inclined configurations. So, it is not surprising to see some previous interests on free convection of nanofluids in inclined porous cavities. Emami et al. [32] discussed the effects of the inclination angle and the hot wall configuration on free convection of nanofluids in a porous cavity. They found that depending on the hot wall position, having the square cavity

inclined may intensify or deteriorate the heat transfer. Rashad et al. [33] analyzed the consequences of size and location of heat sink/source on MHD free convection and entropy generation of nanofluids in an inclined porous cavity. The highest heat transfer was found for the inclination angles ranging from 40 to 50° or 300–310°. Meanwhile, Bondareva et al. [34] undertake a headline visualization study for MHD free convection of nanofluids in an inclined wavy open porous cavity. They observed that an increase in the inclination angle reduces the heat transfer.

In this study, free convection flow and heat transfer of NEPCMs suspension in an inclined porous enclosure are simulated and discussed. The present work tends to address the consequences of the variation of the fusion temperature and the latent heat capacity of encapsulated particles (Stefan number) on the distributions of flow and thermal fields as well as heat transfer characteristics. To the authors' knowledge, this investigation is unique.

2. Problem physics and modelling

2.1. Problem physics

The geometry considered is an inclined porous cavity (H) saturated with a suspension of liquid host fluid and NEPCM particles, as depicted in Fig. 1. The micro-particles-suspensions are involved with the rotation effect of particles, and the shear-rate induced viscosity effects. However, in the nanoscale, the rotation of nanoparticles and its effect on the shear-dependent viscosity is not important and can be neglected. In contrast, at the nanoscale, the magnitude of dynamic viscosity and thermal conductivity of the suspension containing nanoparticles are far from that of containing micron-size particles. Table 1 lists the thermophysical properties of the nanoparticles and the host fluid materials. The fusion temperature of the PCM cores is about 32 °C, while the latent heat is 211 kJ/kg [35].

As indicated in Fig. 1, a heater of the length of l_h and a cooler of the length of l_c are located on the left and right sides of the cavity. Also, the centre of the heater and cooler are set at aH and bH locations, respectively. The other sides of the cavity are thermally impervious.

The inclined cavities heated from side walls have various applications in reactors and energy storage systems. For example, in solar collector cavities, a side of the collector is exposed to solar radiation and is hot, while the other side is in contact with a cold liquid. In the energy storage units, a side of the cavity is connected to a hotline for charging while the other side to a cold line for discharging. The heated/cooled locations of the walls show the location of the placement of heatsinks or the heating/cooling pipes. The insulated portion of walls provides free space for the mechanical placement of the holders of the enclosure. In the case of an array of enclosures, the insulated parts indicate the symmetry line between two similar enclosures. It is assumed that the suspension remains uniform during the natural convection. Moreover, the local temperature of the porous matrix and the suspension are identical, which leads to the local thermal equilibrium heat transfer.

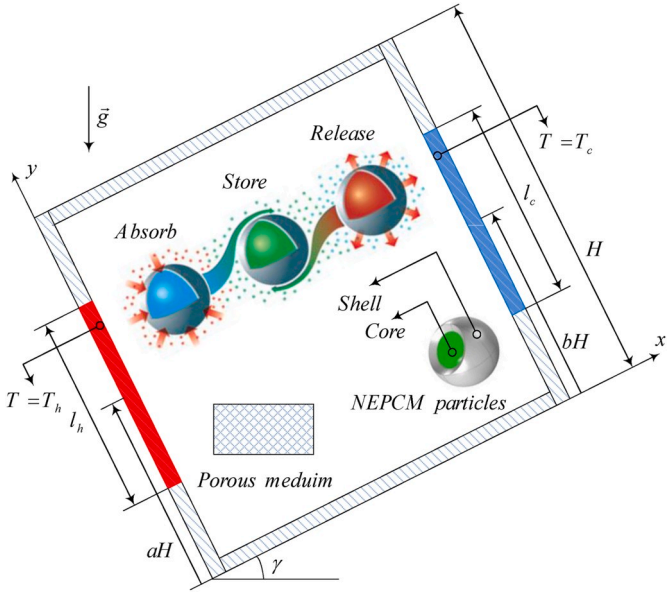

Fig. 1. The schematic configuration of the physical model.

Table 1
Thermophysical properties of the nanoparticles and the host fluid [35,36].

	Material	k (W/m.K)	C (kJ/kg.K)	ρ (kg/m^3)	β (K^{-1})
Core	Nonadecane		1317.7	786	17.28×10^{-5}
Shell	Polyurethane		2037	721	
Host fluid	Water [25 °C]	0.613	4179	997.1	21×10^{-5}
Porous matrix	Glass balls	1.05	840	2700	

2.2. Mathematical formulation

Following the model assumptions, the thermal and hydrodynamic behaviour of the NEPCM-suspension in the porous matrix are introduced as below:

The mass conservation for the suspension

$$\frac{\partial u}{\partial x}+\frac{\partial v}{\partial y}=0 \tag{1}$$

The momentum conservation for the suspension

$$\frac{\rho_b}{\varepsilon^2}\left(u\frac{\partial u}{\partial x}+v\frac{\partial u}{\partial y}\right)=-\frac{\partial p}{\partial x}+\frac{\mu_b}{\varepsilon}\left(\frac{\partial^2 u}{\partial x^2}+\frac{\partial^2 u}{\partial y^2}\right)+g\rho_b\beta_b(T-T_c)\sin(\gamma)-\frac{\mu_b}{K}u \tag{2}$$

$$\frac{\rho_b}{\varepsilon^2}\left(u\frac{\partial v}{\partial x}+v\frac{\partial v}{\partial y}\right)=-\frac{\partial p}{\partial y}+\frac{\mu_b}{\varepsilon}\left(\frac{\partial^2 v}{\partial x^2}+\frac{\partial^2 v}{\partial y^2}\right)+g\rho_b\beta_b(T-T_c)\cos(\gamma)-\frac{\mu_b}{K}v \tag{3}$$

The energy conservation for the suspension

$$(\rho C)_b\left(u\frac{\partial T}{\partial x}+v\frac{\partial T}{\partial y}\right)=k_{m,b}\left(\frac{\partial^2 T}{\partial x^2}+\frac{\partial^2 T}{\partial y^2}\right) \tag{4}$$

where

$$k_{m,b}=(1-\varepsilon)k_s+\varepsilon k_b \tag{5}$$

The subscripts of s, m, and b indicate the solid matrix, the effective properties of porous medium and suspension, and the bulk properties of the suspension, respectively. Following the physical model of Fig. 1, the associated boundary conditions are:

$$u=v=0,\quad T=T_h\ \forall\ x,\quad y\,|\,x=0\ \ \&aH-0.5l_h\le y\le aH+0.5l_h \tag{6a}$$

$$u=v=0,\quad T=T_c\ \forall\ x,\quad y\,|\,x=H\ \ \&\ \ bH-0.5l_c\le y\le bH+0.5l_c \tag{6b}$$

$$u=v=0,\quad \frac{\partial T}{\partial y}=0\ \forall\ x,\quad y\ \left|\begin{array}{l} y=0\ \ \&\ \ 0\le x\le H \\ y=H\ \ \&\ \ 0\le x\le H \\ x=0,\ \ y<aH-0.5l_h\ \&\ \ y>bH+0.5l_h \\ x=H,\ \ y<bH-0.5l_c\ \&\ \ y>bH+0.5l_c \end{array}\right. \tag{6c}$$

2.3. The suspension's properties

The suspension's density is written as a weighted average of the host fluid, *f*, and the nano–encapsulated particles:

$$\rho_b = (1-\varphi)\rho_f + \varphi\rho_p \tag{7}$$

The density of NEPCM particles, i.e. ρ_p, can be obtained based on the densities of the core and shell of the particles [37]:

$$\rho_p = \frac{(1+\iota)\rho_c\rho_s}{\rho_s + \iota\rho_c} \tag{8}$$

Here, ρ_s is the shell's density while ρ_c is PCM core's density. The core-shell weight ratio (ι) for most of NEPCMs is about 0.447. The core's density is adopted as the average of the liquid and solid densities. The following relation is applied to compute the suspension's specific heat capacity:

$$C_b = \frac{(1-\varphi)\rho_f C_f + \varphi\rho_p C_{p,eff}}{\rho_b} \tag{9}$$

The following relation represents the specific heat capacity of NEPCM particles (C_p) in the absence of a phase change [31]:

$$C_{p,eff} = C_p = \frac{(C_c + \iota C_s)\rho_c\rho_s}{(\rho_s + \iota\rho_c)\rho_p} \tag{10}$$

Since the cores undergo a phase change, the energy of the latent heat needs to be included in their specific heat capacity. To this aim, rectangular, triangular, or sinusoidal profiles are available [31]. Since the sinusoidal profile substantially improves the numerical convergence by smoothing the variations of C_c, this profile has been used for the current modelling study that is:

$$C_{p,eff} = C_p + \left\{\frac{\pi}{2}\cdot\left(\frac{h_{sf}}{T_{Mr}} - C_p\right)\cdot\sin\left(\pi\frac{T - T_f + T_{Mr}/2}{T_{Mr}}\right)\right\}\omega \tag{11}$$

with

$$\omega = \begin{cases} 0 & T < T_f - T_{Mr}/2 \\ 1 & T_f - T_{Mr}/2 < T < T_f + T_{Mr}/2 \\ 0 & T > T_f + T_{Mr}/2 \end{cases} \tag{12}$$

and T_f being the fusion temperature and T_{Mr} being a small temperature interval wherein the phase change occurs. Since C_p is very low compared to the h_{sf}/T_{Mr}, the term $(\pi C_p/2)$ can be easily neglected. The suspension's volumetric thermal expansion is evaluated as:

$$\beta_b = (1-\varphi)\beta_f + \varphi\beta_p \tag{13}$$

The below linear relations are employed to evaluate thermal conductivity and dynamic viscosity of the suspension containing the nano–encapsulated particles [38]:

$$\frac{k_b}{k_f} = 1 + Nc\varphi \tag{14}$$

$$\frac{\mu_b}{\mu_f} = 1 + Nv\varphi \tag{15}$$

Here, *Nc* and *Nv* denote the numbers of thermal conductivity and dynamic viscosity, respectively. It is worth noting that these relations are only appropriate for diluted nanofluids with $\varphi \le 0.5\%$. Buongiorno et al. [39] and Venerus et al. [40] performed a comprehensive benchmark investigation of the relation between the thermal conductivity and dynamic viscosity of nanofluids and the volume fraction of nanoparticles. As a part of this benchmark investigation, samples of nanofluids were synthesized in 30 different laboratories around the world, and the thermal conductivity of nanofluids was measured by using various measurement devices. The measurement of dynamic viscosity was a sub-side of the investigations. The outcomes confirmed a linear relationship between the volume fraction of nanoparticles and thermal conductivity and dynamic viscosity.

2.4. Non–dimensional form of the governing equations

The following variations are adopted to transform the governing equations into a non-dimensional formula:

$$X = \frac{x}{H},\quad Y = \frac{y}{H},\quad L_c = \frac{l_c}{H},\quad L_h = \frac{l_h}{H}, U = \frac{uH}{\alpha_f},\quad V = \frac{vH}{\alpha_f}$$
$$P = \frac{pH^2}{\rho_f\alpha_f^2},\quad \theta = \frac{T - T_c}{\Delta T}. \tag{16}$$

where $\Delta T = T_h - T_c$ is the temperature scale. Hence, Eqs. (1)–(3) take the forms of:

$$\frac{\partial U}{\partial X} + \frac{\partial V}{\partial Y} = 0 \tag{17}$$

$$\varepsilon^{-2}\left(\frac{\rho_b}{\rho_f}\right)\left(U\frac{\partial U}{\partial X} + V\frac{\partial U}{\partial Y}\right) = -\frac{\partial P}{\partial X} + Pr\varepsilon^{-1}\left(\frac{\mu_b}{\mu_f}\right)\left(\frac{\partial^2 U}{\partial X^2} + \frac{\partial^2 U}{\partial Y^2}\right) + Ra\cdot Pr\left(\frac{\rho_b}{\rho_f}\right)\left(\frac{\beta_b}{\beta_f}\right)\theta\sin(\gamma) - \frac{Pr}{Da}\left(\frac{\mu_b}{\mu_f}\right)U \tag{18}$$

$$\varepsilon^{-2}\left(\frac{\rho_b}{\rho_f}\right)\left(U\frac{\partial V}{\partial X} + V\frac{\partial V}{\partial Y}\right) = -\frac{\partial P}{\partial Y} + Pr\varepsilon^{-1}\left(\frac{\mu_b}{\mu_f}\right)\left(\frac{\partial^2 V}{\partial X^2} + \frac{\partial^2 V}{\partial Y^2}\right) + Ra\cdot Pr\left(\frac{\rho_b}{\rho_f}\right)\left(\frac{\beta_b}{\beta_f}\right)\theta\cos(\gamma) - \frac{Pr}{Da}\left(\frac{\mu_b}{\mu_f}\right)V \tag{19}$$

with the Prandtl number (*Pr*) and the Rayleigh number (*Ra*), being:

$$Pr = \frac{\mu_f}{\rho_f\alpha_f},\quad Ra = \frac{g\rho_f\beta_f\Delta TH^3}{\alpha_f\mu_f} \tag{20}$$

According to Eqs. (7) and (3), the appeared ratios of the density and thermal expansion coefficient can be expressed as:

$$\frac{\rho_b}{\rho_f} = 1 - \varphi + \varphi\frac{\rho_p}{\rho_f} \tag{21a}$$

$$\frac{\beta_b}{\beta_f} = 1 - \varphi + \varphi\frac{\beta_p}{\beta_f} \tag{21b}$$

Here, the thermal expansion behaviour of the nanoparticles is considered similar to the host fluid, and accordingly, $\beta_b/\beta_f \approx 1$.

Eventually, the dimensionless form of the energy equation, Eq. (4), is achieved:

$$Cr\left(U\frac{\partial\theta}{\partial X} + V\frac{\partial\theta}{\partial Y}\right) = \left(\frac{k_{m,b}}{k_f}\right)\left(\frac{\partial^2\theta}{\partial X^2} + \frac{\partial^2\theta}{\partial Y^2}\right) \tag{22}$$

with

$$Cr = \frac{(\rho C)_b}{(\rho C)_f} = 1 - \varphi + \varphi\lambda + \frac{\varphi}{\delta\, Ste}f \tag{23}$$

$$\frac{k_{m,b}}{k_f} = (1-\varepsilon)\frac{k_s}{k_f} + \varepsilon(1 + Nc\varphi) \tag{24}$$

Herein, *Cr* is the ratio of the sensible heat capacity of the suspension to that of the host fluid. Meanwhile, the heat capacity ratio (λ), the non–dimensional phase change bond (δ), and Stefan number (*Ste*) are presented as:

$$\lambda = \frac{(C_{c,l} + \iota C_s)\rho_c\rho_s}{(\rho C)_f(\rho_s + \iota\rho_c)},\quad \delta = \frac{T_{Mr}}{\Delta T},\quad Ste = \frac{(\rho C)_f\Delta T(\rho_s + \iota\rho_c)}{(h_{sf}\rho_c\rho_s)(1+\iota)} \tag{25}$$

In addition, the function of non–dimensional fusion is defined as:

$$f=\frac{\pi}{2}\sin\left(\frac{\pi}{\delta}(\theta-\theta_f+\delta/2)\right)\sigma \tag{26}$$

with θ_f being the non–dimensional fusion temperature:

$$\theta_f=\frac{T_f-T_C}{\Delta T} \tag{27}$$

and

$$\sigma=\begin{cases}0 & \theta<\theta_f-\delta/2\\ 1 & \theta_f-\delta/2<\theta<\theta_f+\delta/2\\ 0 & \theta>\theta_f+\delta/2\end{cases} \tag{28}$$

Ultimately, below is the dimensionless form of the boundary conditions:

$$U=V=0,\quad \theta=1\ \forall\ X,\quad Y\mid X=0\ \ \&\ \ a-0.5L_h\le Y\le a+0.5L_h \tag{29a}$$

$$U=V=0,\quad \theta=0\ \forall\ X,\quad Y\mid X=1\ \ \&\ \ b-0.5L_c\le Y\le a+0.5L_c \tag{29b}$$

$$U=V=0,\quad \frac{\partial\theta}{\partial Y}=0\ \forall\ X,\quad Y\ \left|\begin{array}{ll} Y=0, & \&\ \ 0\le X\le 1\\ Y=1, & \&\ \ 0\le X\le 1\\ X=0, & Y<a-0.5L_h\ \&\ \ Y>b+0.5L_h\\ X=1, & Y<b-0.5L_c\ \&\ \ Y>b+0.5L_h\end{array}\right. \tag{29c}$$

2.5. Heat transfer characteristics

The local Nusselt number at the heated side wall is obtained by applying the energy balance at the surface:

$$Nu_Y=-\frac{k_{m,\,b}}{k_f}\left(\frac{\partial\theta}{\partial X}\right)\mid X=0\ \&\ a-0.5L_h\le Y\le a+0.5L_h \tag{30}$$

where $k_{m,b}/k_f$ was defined in Eq. (24). The integration of the above equations gives the average Nusselt number:

$$Nu=\frac{1}{L_h}\int_{a-0.5L_h}^{a+0.5L_h}Nu_Y\,dY \tag{31}$$

In order to study the advantage of using NEPCM particles, the normalized average Nusselt number ($NNu_{\varphi=0}$) is defined:

$$NNu_{\varphi=0}=\frac{Nu}{Nu_{\varphi=0}} \tag{32}$$

where $Nu_{\varphi=0}$ belongs to the case with no NEPCMs. Finally, it should be noted that the presence of the NEPCM particles changes the thermal conductivity, dynamic viscosity, density ratio, and other thermophysical properties of the working fluid. The Nusselt number is normalized with a case having no phase change (i.e., with $Ste\to\infty$) to introduce the normalized Nusselt number as:

$$NNu_{Ste\to\infty}=\frac{Nu}{Nu_{Ste\to\infty}} \tag{33}$$

The above equation shows the impact of the latent heat of the particles on the heat transfer performance.

3. Numerical approach, grid check, and verification

The finite element method [41,42] was applied to integrate the set of governing equations of Eqs. (17)–(19) and (22). The continuity equation was satisfied using a penalty parameter ($\chi>10^7$) in the momentum equations, as discussed by Reddy [42]:

$$P=-\chi\left(\frac{\partial U}{\partial X}+\frac{\partial V}{\partial Y}\right) \tag{34}$$

$$\varepsilon^{-2}\left(\frac{\rho_b}{\rho_f}\right)\left(U\frac{\partial U}{\partial X}+V\frac{\partial U}{\partial Y}\right)=\frac{\partial}{\partial X}\left[\chi\left(\frac{\partial U}{\partial X}+\frac{\partial V}{\partial Y}\right)\right]+Pr\varepsilon^{-1}\left(\frac{\mu_b}{\mu_f}\right)\left(\frac{\partial^2U}{\partial X^2}+\frac{\partial^2U}{\partial Y^2}\right)+Ra\cdot Pr\left(\frac{\rho_b}{\rho_f}\right)\theta\sin(\gamma)-\frac{Pr}{Da}\left(\frac{\mu_b}{\mu_f}\right)\left(\frac{\rho_b}{\rho_f}\right)U \tag{35}$$

$$\varepsilon^{-2}\left(\frac{\rho_b}{\rho_f}\right)\left(U\frac{\partial V}{\partial X}+V\frac{\partial V}{\partial Y}\right)=-\frac{\partial}{\partial Y}\left[\chi\left(\frac{\partial U}{\partial X}+\frac{\partial V}{\partial Y}\right)\right]+Pr\varepsilon^{-1}\left(\frac{\mu_b}{\mu_f}\right)\left(\frac{\partial^2V}{\partial X^2}+\frac{\partial^2V}{\partial Y^2}\right)+Ra\cdot Pr\left(\frac{\rho_b}{\rho_f}\right)\theta\cos(\gamma)-\frac{Pr}{Da}\left(\frac{\mu_b}{\mu_f}\right)\left(\frac{\rho_b}{\rho_f}\right)V \tag{36}$$

Then, the velocities (U and V), as well as the temperature (θ), were expanded utilizing a basis set $\{\zeta_k\}_{k=1}^N$ as:

$$U\approx\sum_{k=1}^{N}(U)_k\zeta_k(X,Y),\quad V\approx\sum_{k=1}^{N}(V)_k\zeta_k(X,Y),\quad \theta\approx\sum_{k=1}^{N}\theta_k\zeta_k(X,Y) \tag{37}$$

in the domain of the solution. The Galerkin FEM was employed to achieve the corresponding non–linear residual equations at the internal elements:

$$\begin{aligned}R_i^{(1)}=&\varepsilon^{-2}\left(\frac{\rho_b}{\rho_f}\right)\sum_{k=1}^{N}U_k\int_\Omega\left[\left(\sum_{k=1}^{N}U_k\zeta_k\right)\frac{\partial\zeta_k}{\partial X}+\left(\sum_{k=1}^{N}V_k\zeta_k\right)\frac{\partial\zeta_k}{\partial Y}\right]\zeta_i dXdY\\&+\chi\left[\sum_{k=1}^{N}U_k\int_\Omega\frac{\partial\zeta_i}{\partial X}\frac{\partial\zeta_k}{\partial X}dXdY+\sum_{k=1}^{N}V_k\int_\Omega\frac{\partial\zeta_i}{\partial X}\frac{\partial\zeta_k}{\partial Y}dXdY\right]\\&+Pr\varepsilon^{-1}\left(\frac{\mu_b}{\mu_f}\right)\sum_{k=1}^{N}U_k\int_\Omega\left[\frac{\partial\zeta_i}{\partial X}\frac{\partial\zeta_k}{\partial X}+\frac{\partial\zeta_i}{\partial Y}\frac{\partial\zeta_k}{\partial Y}\right]dXdY\\&-\frac{Pr}{Da}\left(\frac{\mu_b}{\mu_f}\right)\sum_{k=1}^{N}\int_\Omega\left(\sum_{k=1}^{N}U_k\zeta_k\right)\zeta_i dXdY\\&+RaPr\left(\frac{\rho_b}{\rho_f}\right)\left[\int_\Omega\left(\sum_{k=1}^{N}\theta_k\zeta_k\right)\zeta_i dXdY\right]\sin(\gamma)\end{aligned} \tag{38}$$

$$\begin{aligned}R_i^{(2)}=&\varepsilon^{-2}\left(\frac{\rho_b}{\rho_f}\right)\sum_{k=1}^{N}V_k\int_\Omega\left[\left(\sum_{k=1}^{N}U_k\zeta_k\right)\frac{\partial\zeta_k}{\partial X}+\left(\sum_{k=1}^{N}V_k\zeta_k\right)\frac{\partial\zeta_k}{\partial Y}\right]\zeta_i dXdY\\&+\chi\left[\sum_{k=1}^{N}U_k\int_\Omega\frac{\partial\zeta_i}{\partial Y}\frac{\partial\zeta_k}{\partial X}dXdY+\sum_{k=1}^{N}V_k\int_\Omega\frac{\partial\zeta_i}{\partial Y}\frac{\partial\zeta_k}{\partial Y}dXdY\right]\\&+Pr\varepsilon^{-1}\left(\frac{\mu_b}{\mu_f}\right)\sum_{k=1}^{N}V_k\int_\Omega\left[\frac{\partial\zeta_i}{\partial X}\frac{\partial\zeta_k}{\partial X}+\frac{\partial\zeta_i}{\partial Y}\frac{\partial\zeta_k}{\partial Y}\right]dXdY\\&-\frac{Pr}{Da}\left(\frac{\mu_b}{\mu_f}\right)\sum_{k=1}^{N}\int_\Omega\left(\sum_{k=1}^{N}V_k\zeta_k\right)\zeta_i dXdY\\&+RaPr\left(\frac{\rho_b}{\rho_f}\right)\left[\int_\Omega\left(\sum_{k=1}^{N}\theta_k\zeta_k\right)\zeta_i dXdY\right]\cos(\gamma)\end{aligned} \tag{39}$$

$$\begin{aligned}R_i^{(3)}=&\sum_{k=1}^{N}Cr\theta_k\int_\Omega\left[\left(\sum_{k=1}^{N}U_k\zeta_k\right)\frac{\partial\zeta_k}{\partial X}+\left(\sum_{k=1}^{N}V_k\zeta_k\right)\frac{\partial\zeta_k}{\partial Y}\right]\zeta_i dXdY\\&+\left(\frac{k_{m,\,b}}{k_f}\right)\left(\sum_{k=1}^{N}\theta_k\int_\Omega\left[\frac{\partial\zeta_i}{\partial X}\frac{\partial\zeta_k}{\partial X}+\frac{\partial\zeta_i}{\partial Y}\frac{\partial\zeta_k}{\partial Y}\right]dXdY\right)\end{aligned} \tag{40}$$

The integrations were numerically computed by using biquadratic functions along with the three-point Gaussian quadrature. Then, the Newton–Raphson technique was applied to find the coefficients of

Table 2
Grid independence assessment when $Ste = 0.2$, $\theta_f = 0.3$, $\varphi = 0.05\%$, $\gamma = 45°$.

Number of elements	*Nu*	*Error* (%)	Ψ_{Max}	*Error* (%)
50 × 50	6.0846	–	3.8914	–
75 × 75	6.0802	0.072	3.8901	0.033
100 × 100	6.0762	0.066	3.8890	0.028
125×125	**6.0744**	**0.030**	**3.8885**	**0.012**
150 × 150	6.0730	0.023	3.8881	0.011

The bold line was adopted for numerical computations of the present study.

Table 3
The average Nu computed in the current work and those presented in Kahveci [43] when $Ra = 10^6$.

	$\varphi = 0.0$	$\varphi = 0.05$	$\varphi = 0.1$	$\varphi = 0.15$	$\varphi = 0.2$
Present study	9.20	9.76	10.3	10.8	11.2
Kahveci [43]	9.23	9.783	10.297	10.771	11.206

Table 4
The average Nu in a porous medium filled with *Cu*-water nanofluid when $Ra \times Da = 10^3$.

φ	Present work	Sun and Pop [44]	Sheremet et al. [45]
0.1	9.42	9.42	9.41
0.2	12.85	12.85	12.84

expansions, i.e., U_k, V_k, and θ_k. The residual equations were iteratively solved until the residual error reaches 10^{-6}.

The influence of the mesh size on the numerical accuracy was explored by repeating he computations for different mesh sizes. Results are reported in Table 2. Notice that the 125 × 125 grid system is suitable for the current simulations.

The accuracy of the present code is validated thoroughly by comparisons of the results with the literature studies [43–46]. Tables 3 and 4 as well as Figs. 2 and 3 show theses evaluations. As clearly seen, the utilized code is correct and accurate.

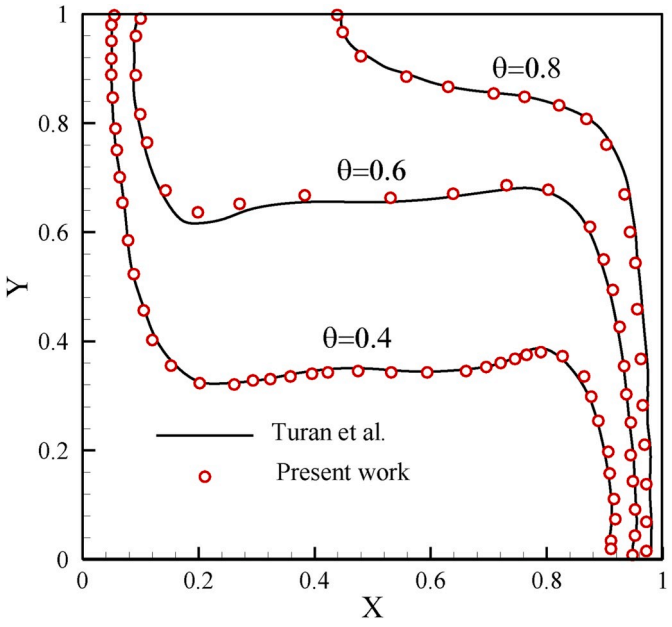

Fig. 2. The temperature distribution computed in the current study and those reported by Turan et al. [46].

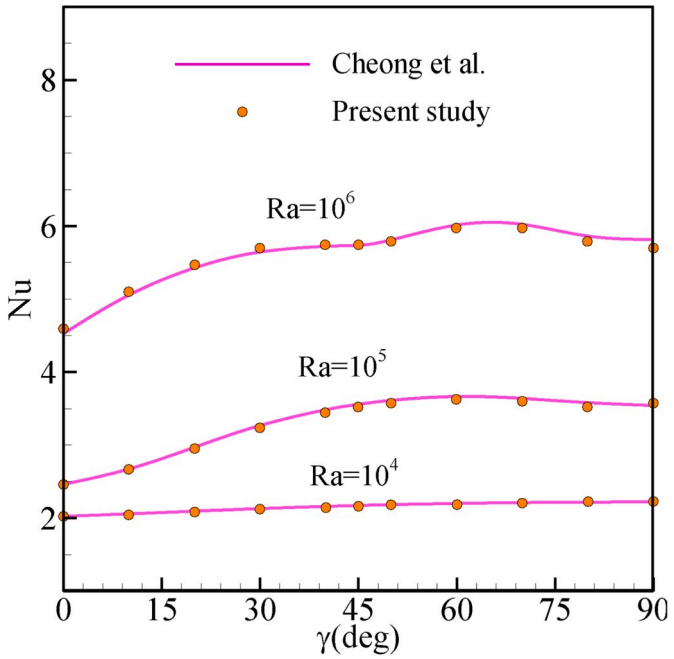

Fig. 3. Average Nu of the current work and the study of Cheong et al. [47].

4. Simulation results

The simulation results describing the thermal and hydrodynamic behaviors of a suspension containing the NEPCM particles are presented in this section. The studied key parameters are: inclination angle of the cavity $0° \le \gamma \le 90°$, Stefan number $0.2 \le Ste \le \infty$, non–dimensional fusion temperature $0.05 \le \theta_f \le 0.95$, and the volume fraction of the particles $0.0 \le \varphi \le 5\%$ While, the constant parameters are $Ra = 10^6$, $Nv = 12.5$, $Nc = 23.8$, $Da = 10^{-4}$, $\varepsilon = 0.9$, $Pr = 6.2$, $k_s/k_f = 1.713$, $a = b = 0.5$, $L_c = L_h = 0.4$ and $\lambda = 0.322$.

In what concerns the distributions of streamlines, isotherms, and heat capacity ratio of the suspension to the host liquid, i.e., *Cr*, simulation results are presented in Figs. 4–6 that correspond to $Ste = 0.2$, and $\varphi = 0.05$. In these figures, the dependency of the simulation results on the fusion temperature and the inclination angle of the cavity is examined by providing the contour plots for different values of these parameters (i.e. $\theta_f = 0.05$, 0.35, 0.65, 0.95 and $\gamma = 0°$, 30°, 60°, and 90°).

When the inclination angle is in the range of $0° \le \gamma \le 60°$, Fig. 4 shows that arise in the inclination angle of the cavity does not change the general shape of the streamlines; a single rotating cell, regardless of the value of θ_f, appears in the cavity with an ascending flow near the left wall and a descending flow near the right. In fact, the suspension in the vicinity of the partially hot wall is heated, leading to a decrease in its density; then, the buoyancy force induced by the variations of the density moves the suspension upward along the hot wall. In the following, after passing from one end of the adiabatic upper bound, the suspension reaches the partially cold wall. On the other hand, the suspension is cooled near the partially cold wall and moves downward, and it flows along the bottom insulated wall towards the hot wall. Thus, a clockwise vortex appears in the enclosure. However, four rotating cells appear in the cavity when the inclination angle reaches 90°. The cells in the bottom–left/top–right parts of the cavity are rotating counterclockwise, but those in the bottom–right/top–left parts are clockwise. When the inclination angle is 90°, the applied buoyancy forces are symmetrical with respect to the vertical line passing the centre of the cavity. Thus, the formation of a symmetric flow inside the cavity is predictable. However, the physics of the problem is not symmetric for other inclination angles. In these cases, the buoyancy force is divided into two components; one along the hot wall and other normal to it.

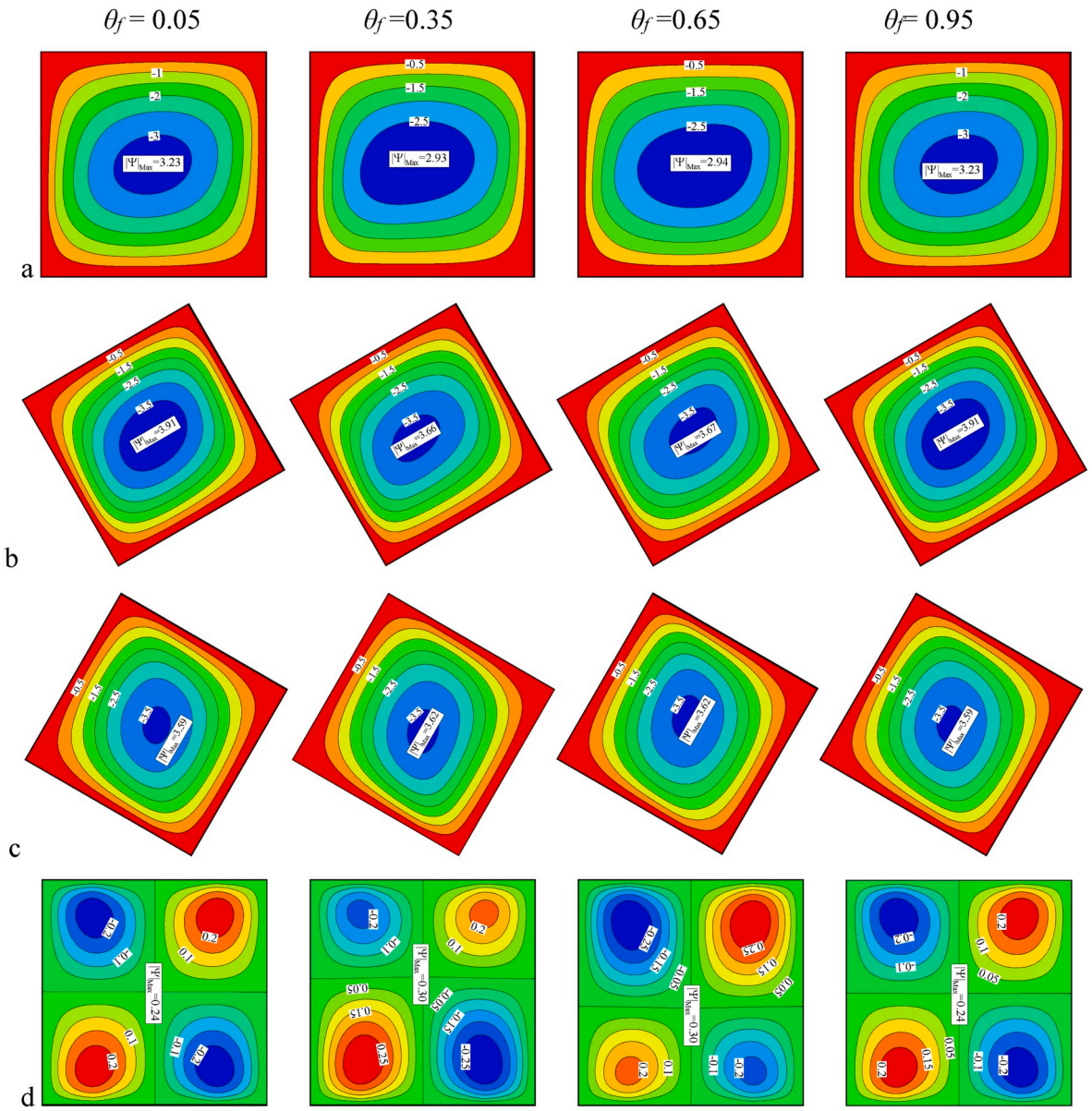

Fig. 4. Dependecy of the streamlines to the fusion temperature for selected inclination angles (a): $\gamma = 0°$, (b): $\gamma = 30°$, (c): $\gamma = 60°$, and (d): $\gamma = 90°$ at $Ste = 0.2$, and $\varphi = 0.05$.

A non-symmetric force causes a non-symmetric flow. Therefore, differences between the governing fields of the cavity with the inclination angle of 90° and other cavities can be attributed to this fact. Notice that the highest flow strength, Ψ_{max}, belongs to $\gamma = 30°$ followed by $\gamma = 60°$ while the values of flow strength for $\gamma = 90°$ is considerably lower. As already mentioned, when the inclination angle is in the range of $0° < \gamma < 90°$, the buoyancy force vector has two components; one component, i.e. $Ra{\cdot}Pr\left(\frac{\rho_b}{\rho_f}\right)\left(\frac{\beta_b}{\beta_f}\right)\theta\cos(\gamma)$, causes the suspension to moves along the hot wall and other, i.e., $Ra{\cdot}Pr\left(\frac{\rho_b}{\rho_f}\right)\left(\frac{\beta_b}{\beta_f}\right)\theta\sin(\gamma)$, pushes the fluid along the insulated walls. In fact, the second component of the buoyancy force facilities and accelerate the free convection. The first and second components of the buoyancy force, respectively, weaken and strengthen while increasing the inclination angle. As the results show, the interaction between these components on the flow strength is optimum at $\gamma = 30°$.

Comparison of the results of different fusion temperatures indicates that for $\gamma = 0°$ and 30°, the highest flow strengths belong to $\theta_f = 0.05$ and 0.95. However, for higher values of the inclination angle, this occurs for $\theta_f = 0.35$ and 0.65. This indicates that the effect of non–dimensional fusion temperature on the flow strength varies with the inclination angle of the cavity.

Fig. 5 indicates that temperature distribution for $\gamma = 0°$, 30° and 60° are almost identical; and substantially different from $\gamma = 90°$. As previously explained in details, the physics of the problem is symmetrical when $\gamma = 90°$; consequently, the governing fields such as the temperature one is symmetry. On the other hand, it can be seen that the temperature fields follow the corresponding flow patterns so that the distortion of the isotherms increases as the flow strength augments. A more detailed look shows that the fusion temperature can affect the isotherms. As a matter of fact, the isothermal surface is found to expand around the corresponding isotherm of the fusion temperature. In fact, in this area, the core of the NEPCM particles stored the heat without a noticeable increase in temperature.

The particles are suspended in the liquid and circulate with the liquid in the cavity. The NEPCM-suspension absorbs the heat and expands, hence due to the buoyancy force, the fluid tends to move upward along

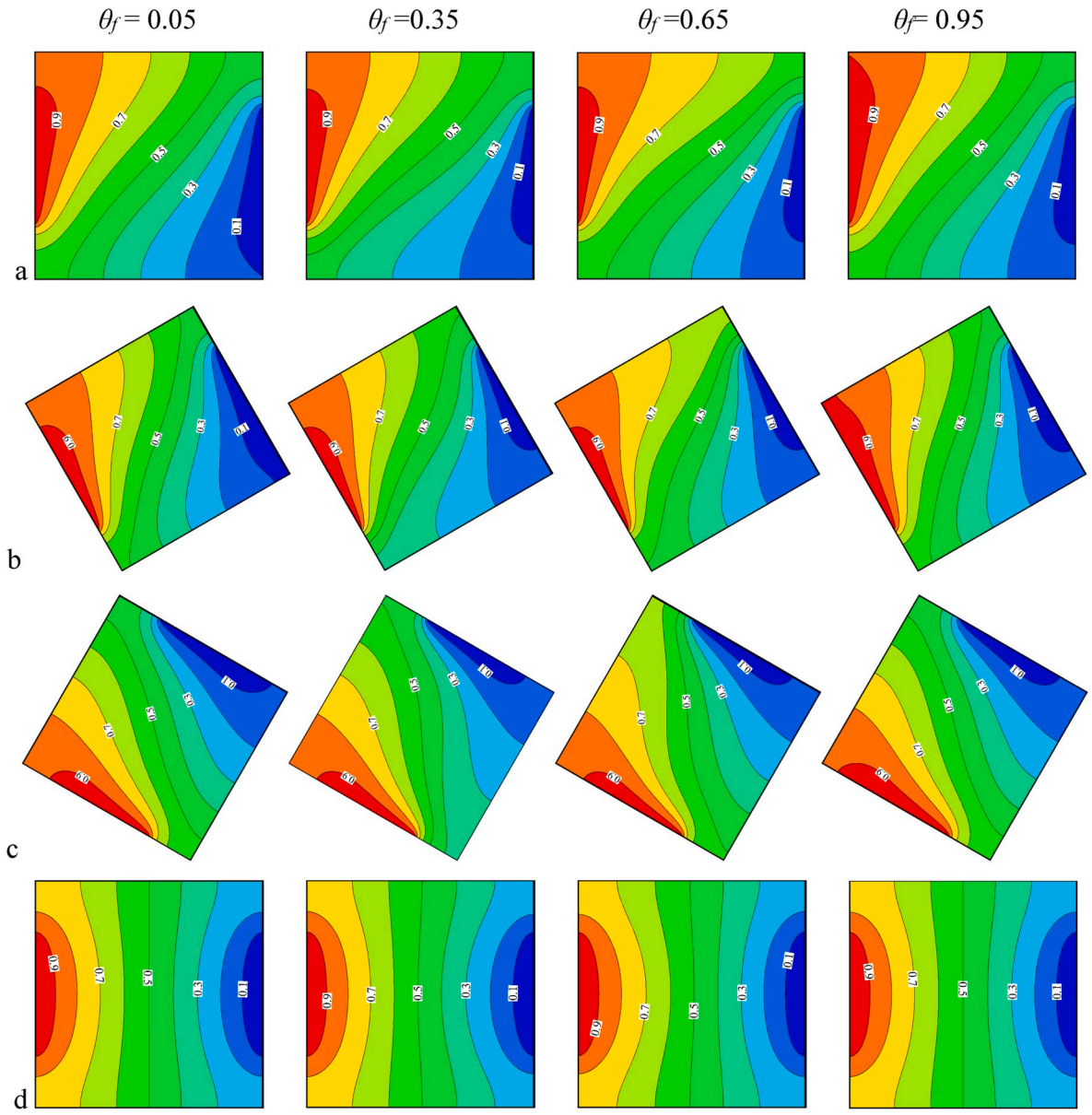

Fig. 5. Dependecy of the isotherms to the fusion temperature for selected inclination angles (a): $\gamma = 0°$, (b): $\gamma = 30°$, (c): $\gamma = 60°$, and (d): $\gamma = 90°$ at $Ste = 0.2$, and $\varphi = 0.05$.

the top insulated wall. When the suspension reaches the cold wall, it loses some of its energy and contracts. The contracted suspension is heavy and moves downward.

Here, the investigated problem is steady-state, but the NEPCM particles circulate in the cavity along with the liquid. Hence, they could experience hot and cold regions. When the nanoparticles enter a region with a temperature higher than their fusion temperature, they phase change to a molten state by absorbing latent heat. As soon as the molten nanoparticles enter a region colder than their fusion temperature, they release the latent heat and phase change to a solidus state. Although the problem under investigation is a steady-state problem, there are regions with phase change due to the circulation of nanoparticles.

Deviation of the heat capacity ratio from 0.97 is attributed to the latent heat of the phase change of the core of NEPCM particles. So, the ribbon zones in Fig. 6 indicate the regions wherein the nanoparticle's core undergo a phase change, called melting-solidification zones. The particles suspended on the left of the melting-solidification zone are wholly melted. However, the nanoparticles on the other side of the ribbon are completely solidified. The NEPCM particles release/absorb the latent heat while arriving in the solidification/melting zone. By increasing the fusion temperature from 0.05 to 0.35, the melting-solidification ribbon extends and moves away from the cold surface. Moreover, the areas of the solidification and melting zones, respectively, increase and decrease with the increment in fusion temperature from 0.05 to 0.35. Consequently, according to the flow paths, more nanoparticles experience the phase change process.

For $\theta_f = 0.35$ or 0.65, the phase change appears in a larger area in the cavity compared to the phase change zones of $\theta_f = 0.05$ and 0.95. Also, it can be seen the *Cr* fields for $\gamma = 0°$, 30° and 60° are somewhat similar but different from $\gamma = 90°$. These discrepancies can be attributed to the temperature fields. In fact, for a specified fusion temperature, the expansion of the phase change zone is determined by the temperature-constant region around the isotherms corresponding to the fusion temperature. Regarding the flow paths, shown in Fig. 4, when $\gamma = 0°$–60°, the number of nanoparticles experiencing the phase change process is approximately the same and sharply

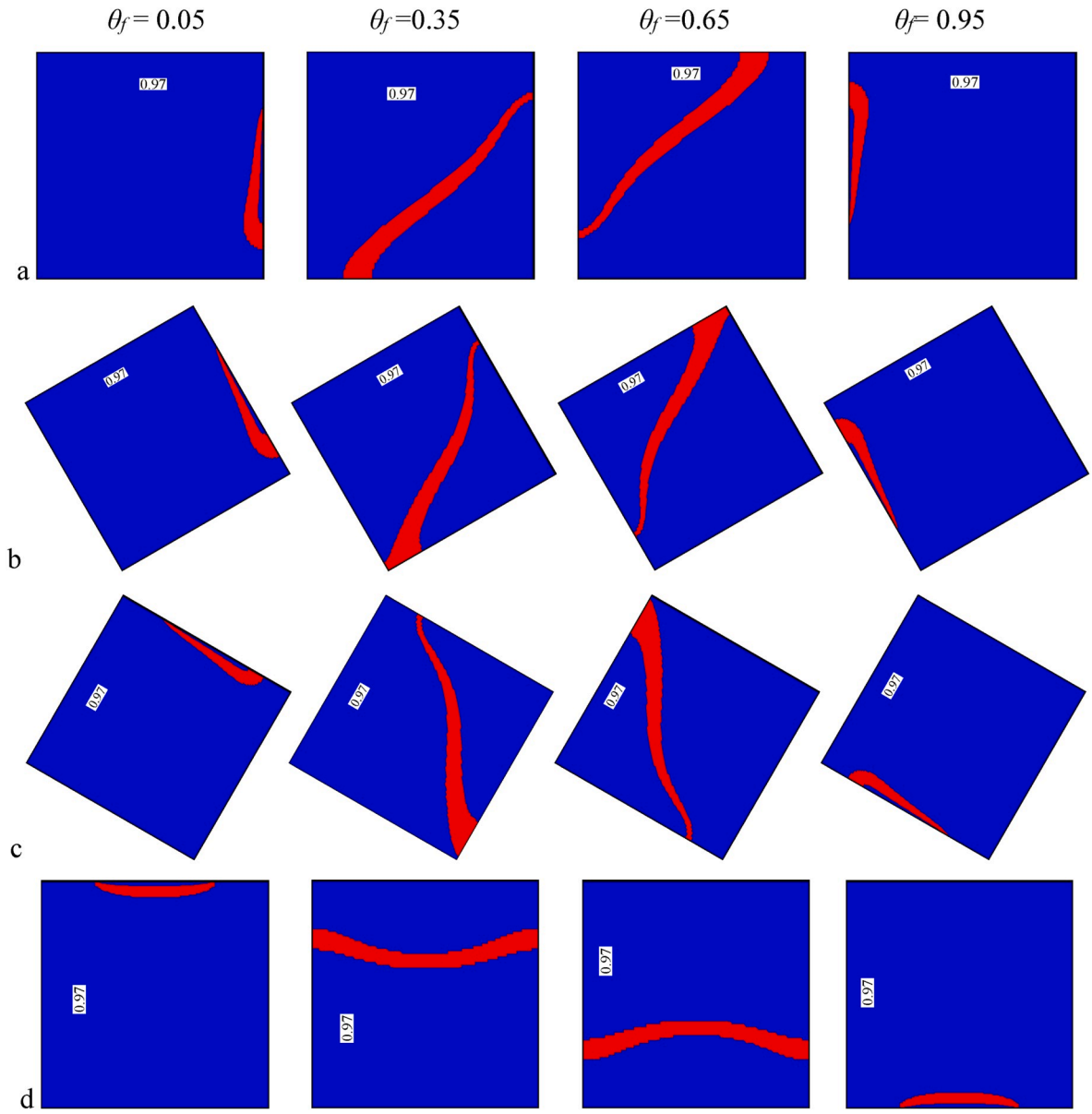

Fig. 6. Dependecy of the *Cr* contours to the fusion temperature for selected inclination angles (a): $\gamma = 0°$, (b): $\gamma = 30°$, (c): $\gamma = 60°$, and (d): $\gamma = 90°$ at $Ste = 0.2$, and $\varphi = 0.05$.

diminishes for $\gamma = 90°$. Hence, a part of the decline in the heat transfer rate in the case of $\gamma = 90°$ can be attributed to this.

Fig. 7 is plotted to analyze the influence of the fusion temperature (θ_f) and the Stefan number (*Ste*) on the average Nusselt number at various inclination angles of the cavity (γ). In Fig. 7(a) the average Nusselt number shows asymmetric behaviour with respect to $\theta_f = 0.5$ for all inclination angles, wherein maximum heat transfer occurs. In fact, when $\theta_f = 0.5$, the areas of the melting and solidification zones are approximately equal. This means that a supreme number of particles experience the phase change process. In other words, the highest amount of latent energy can be transferred when $\theta_f = 0.5$.

Fig. 7(a) and (b) indicate that for $0.05 \leq \theta_f \leq 0.95$ and $0.2 \leq Ste \leq 1$, respectively, the maximum heat transfer performance belongs to the inclination angle of 42°. It is worth noting that the *Ste* and θ_f for Fig. 7(a) and (b) are 0.2 and 0.35. As previously mentioned, by tilting the cavity, the buoyancy force is divided into two components; the first component elevate the suspension along the partially hot wall and decreases with an increase in the inclination angle, the other one moves the fluid along the insulated walls and increases while increasing the inclination angle. The interaction between these components on the heat transfer rate is optimum when $\gamma = 42°$. Fig. 7(b), presented for $\theta_f = 0.35$ and $\varphi = 0.05$, shows that for all of the inclination angles, a decrease in the Stefan number improves the heat transfer. The Stefan number, i.e., *Ste*, is defined as the ratio of sensible heat to latent heat. Hence, considering a constant temperature scale (ΔT), a reduction in the Stefan number is equivalent to a rise in the latent heat (i.e., heat storage capacity) of the NEPCM cores. Thus, the NEPCM particles absorb and then release more heat energy for the lower values of *Ste*.

Here, the effects of the presence of the NEPCM particles on the heat transfer performance will be analyzed. To this aim, variations of *Nu* and $NNu_{\varphi=0}$ versus fusion temperature for different values of the volume fraction of NEPCM particles are plotted in Fig. 8(a) and (b). Excluding the cases with $\theta_f \leq 0.1$ and $\theta_f \geq 0.9$, these figures show that the presence of the particles leads to heat transfer enhancement. Dispersing the particles in the host liquid changes the thermophysical properties of the fluid, including thermal conductivity, dynamic viscosity and the effective heat capacity. An increase in thermal conductivity and heat capacity

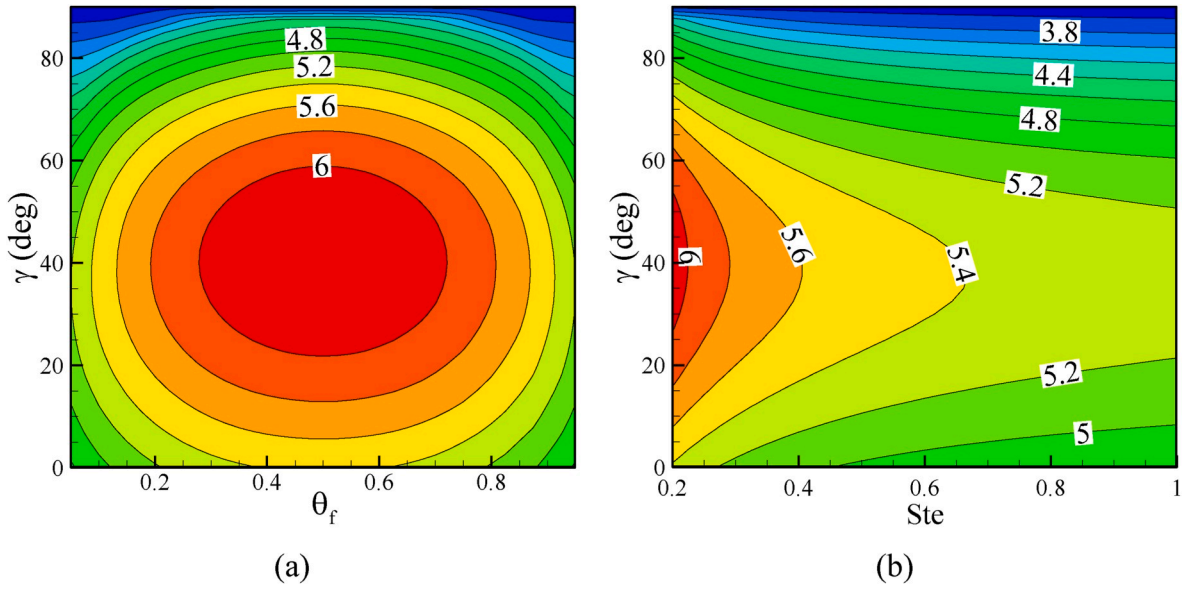

Fig. 7. The dependency of *Nu* on (a): fusion temperature and (b) Stefan number for various values of the inclination angle.

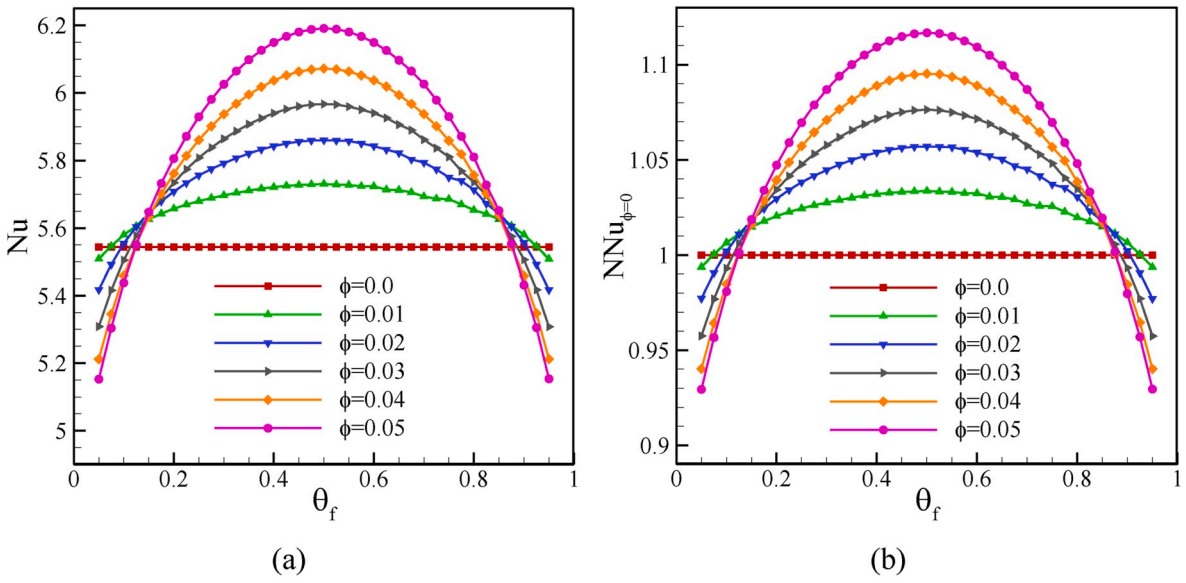

Fig. 8. Variations of (a): *Nu* and (b): $NNu_{\varphi=0}$ versus fusion temperature for various volume fractions of particles when $Ste = 0.2$.

can increase the heat transfer rate. Nonetheless, the heat transfer rate through the convection mechanisms can be reduced due to the increase of the dynamic viscosity with adding NEPCM particles to the base fluid. When $\theta_f \leq 0.1$ and $\theta_f \geq 0.9$, the decreasing effects of NEPCM particles on the rate of heat transfer, due to the increment of the dynamic viscosity, dominates the increasing effects of the presence of the NEPCM particles as a result of the increase in thermal conductivity and effective heat capacity. As shown in Fig. 8(b), up to about 13% increase in the average Nusselt number is observed for $\varphi = 0.05$ and $\theta_f = 0.5$. The calculated percentage can be obtained by the definition of $NNu_{\varphi=0}$ and its value, i.e. $NNu_{\varphi=0} = 1.13$.

Finally, the influence of the phase change of the particle's core on the corresponding heat transfer is discussed. To this aim, results in terms of $NNu_{Ste\to\infty}$ for different values of the fusion temperature, the Stefan number, and the inclination angle of the cavity are provided in Fig. 9(a) and (b). Notice that the phase change of the NEPCM particles may bring up to about 28% enhancement in the heat transfer, as pictured in Fig. 9 (a). Closer scrutiny of the figures indicates that this effect is more remarkable for $\theta_f = 0.5$ or $\gamma = 82^\circ$.

5. Conclusion

Free convection heat transfer of a suspension of nano–encapsulated nonadecane within polyurethane shells dispersed into the water in an inclined porous cavity was analyzed in this study. The FEM was employed to solve the model equations. Several comparisons with the literature results were applied, and the outcomes were found in good agreement. The effects of the fusion temperature and the Stefan number of NEPCM particles on the free convection heat transfer behaviour of NEPCMs in a cavity was investigated at different inclination angles. The conclusions can be summarized as follows:

(1) A decrease in the Stefan number improves the heat transfer rate.
(2) The best heat transfer performance belongs to the inclination angle of 42°. However, at the inclination angle of 82°, the effect

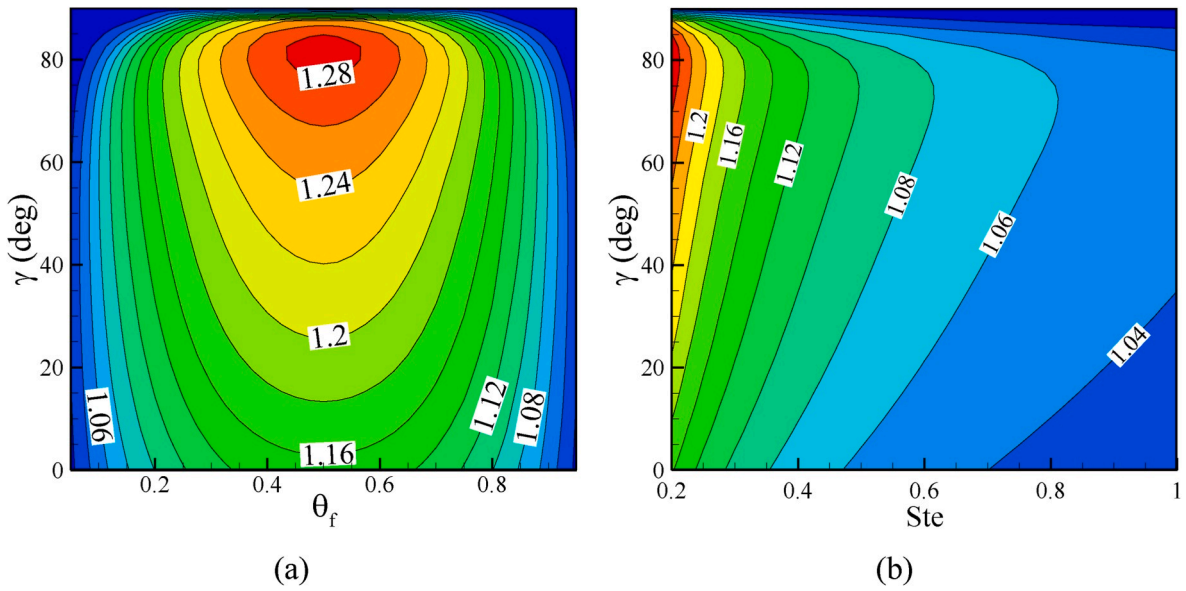

Fig. 9. The dependency of $NNu_{Ste\to\infty}$ to the θ_f and the *Ste* for selected values of the inclination angle when $\varphi = 0.05$; (a): fusion temperature when $Ste = 0.2$, and (b): Stefan number when $\theta_f = 0.35$.

of the core phase change of the NEPCM particles attains its maximum value.

(3) The presence of the NEPCM particles leads to about 13% heat transfer improvement, and the maximum heat transfer occurs at $\theta_f = 0.5$.

(4) The phase change of the NEPCM particles may bring up to about 28% enhancement in the heat transfer.

The results showed that there was an optimized value of fusion temperature at the fusion temperature about $\theta_f = 0.5$, which was the middle range of phase change temperature band (0–1). It was also clear that the phase change was a function of temperature and almost followed the temperature patterns. Since the geometry of the cavity and the adopted temperature boundary conditions led to semi-symmetric flow and heat transfer in the enclosure, the optimum fusion temperature of $\theta_f = 0.5$ could be due to this semi-symmetric effect. Hence, the study of NEPCMs heat transfer in complex non-symmetric geometries can be investigated in future works.

Declaration of competing interest

The authors clarify that there is no conflict of interest for report.

Appendix A. Supplementary data

Supplementary data to this article can be found online at https://doi.org/10.1016/j.ijthermalsci.2020.106503.

References

[1] R.A. Mahdi, H. Mohammed, K. Munisamy, N. Saeid, Review of convection heat transfer and fluid flow in porous media with nanofluid, Renew. Sustain. Energy Rev. 41 (2015) 715–734.
[2] A. Kasaeian, R. Daneshazarian, O. Mahian, L. Kolsi, A.J. Chamkha, S. Wongwises, I. Pop, Nanofluid flow and heat transfer in porous media: a review of the latest developments, Int. J. Heat Mass Tran. 107 (2017) 778–791.
[3] Y. Menni, A.J. Chamkha, A. Azzi, Nanofluid transport IN porous media: a review, special topics & reviews in porous media, Int. J. 10 (2019).
[4] A.I. Alsabery, R. Mohebbi, A.J. Chamkha, I. Hashim, Effect of local thermal non-equilibrium model on natural convection in a nanofluid-filled wavy-walled porous cavity containing inner solid cylinder, Chem. Eng. Sci. 201 (2019) 247–263.
[5] S. Mehryan, M.A. Sheremet, M. Soltani, M. Izadi, Natural convection of magnetic hybrid nanofluid inside a double-porous medium using two-equation energy model, J. Mol. Liq. 277 (2019) 959–970.
[6] A.J. Chamkha, S. Sazegar, E. Jamesahar, M. Ghalambaz, Thermal non-equilibrium heat transfer modeling of hybrid nanofluids in a structure composed of the layers of solid and porous media and free nanofluids, Energies 12 (2019) 541.
[7] I. Zahmatkesh, M.R. Habibi, Natural and mixed convection of a nanofluid in porous cavities: critical analysis using Buongiorno's model, J. Theor. Appl. Mech. 57 (2019) 221–233.
[8] T. Tayebi, A.J. Chamkha, M. Djezzar, Natural convection of CNT-water nanofluid in an annular space between confocal elliptic cylinders with constant heat flux on inner wall, Scientia Iranica. Trans. B, Mech. Eng. 26 (2019) 2770–2783.
[9] M.S. Ishak, A.I. Alsabery, A. Chamkha, I. Hashim, Effect of finite wall thickness on entropy generation and natural convection in a nanofluid-filled partially heated square cavity, Int. J. Numer. Methods Heat Fluid Flow 30 (3) (2019) 1518–1546.
[10] M.A. Sheremet, I. Pop, A.C. Baytas, Non-equilibrium natural convection in a differentially-heated nanofluid cavity partially filled with a porous medium, Int. J. Numer. Methods Heat Fluid Flow 29 (8) (2019) 2524–2544.
[11] A. Alsabery, A. Chamkha, H. Saleh, I. Hashim, Heatline visualization of conjugate natural convection in a square cavity filled with nanofluid with sinusoidal temperature variations on both horizontal walls, Int. J. Heat Mass Tran. 100 (2016) 835–850.
[12] Y. Zhu, Y. Qin, S. Liang, K. Chen, C. Tian, J. Wang, X. Luo, L. Zhang, Graphene/SiO2/n-octadecane nanoencapsulated phase change material with flower like morphology, high thermal conductivity, and suppressed supercooling, Appl. Energy 250 (2019) 98–108.
[13] J. Shi, X. Wu, R. Sun, B. Ban, J. Li, J. Chen, Nano-encapsulated phase change materials prepared by one-step interfacial polymerization for thermal energy storage, Mater. Chem. Phys. 231 (2019) 244–251.
[14] A. Jamekhorshid, S. Sadrameli, M. Farid, A review of microencapsulation methods of phase change materials (PCMs) as a thermal energy storage (TES) medium, Renew. Sustain. Energy Rev. 31 (2014) 531–542.
[15] W. Su, J. Darkwa, G. Kokogiannakis, Review of solid–liquid phase change materials and their encapsulation technologies, Renew. Sustain. Energy Rev. 48 (2015) 373–391.
[16] C. Liu, Z. Rao, J. Zhao, Y. Huo, Y. Li, Review on nanoencapsulated phase change materials: preparation, characterization and heat transfer enhancement, Nano Energy 13 (2015) 814–826.
[17] N.S. Bondareva, B. Buonomo, O. Manca, M.A. Sheremet, Heat transfer performance of the finned nano-enhanced phase change material system under the inclination influence, Int. J. Heat Mass Tran. 135 (2019) 1063–1072.
[18] K. Hosseinzadeh, M. Alizadeh, D. Ganji, Solidification process of hybrid nano-enhanced phase change material in a LHTESS with tree-like branching fin in the presence of thermal radiation, J. Mol. Liq. 275 (2019) 909–925.
[19] R.P. Singh, H. Xu, S. Kaushik, D. Rakshit, A. Romagnoli, Charging performance evaluation of finned conical thermal storage system encapsulated with nano-enhanced phase change material, Appl. Therm. Eng. 151 (2019) 176–190.
[20] M. Martín, A. Villalba, A.I. Fernández, C. Barreneche, Development of new nano-enhanced phase change materials (NEPCM) to improve energy efficiency in buildings: lab-scale characterization, Energy Build. 192 (2019) 75–83.
[21] K.Y. Leong, M.R. Abdul Rahman, B.A. Gurunathan, Nano-enhanced phase change materials: a review of thermo-physical properties, applications and challenges, J. Energy Storage 21 (2019) 18–31.
[22] W. Wu, H. Bostanci, L. Chow, Y. Hong, C. Wang, M. Su, J.P. Kizito, Heat transfer enhancement of PAO in microchannel heat exchanger using nano-encapsulated phase change indium particles, Int. J. Heat Mass Tran. 58 (2013) 348–355.

[23] H.R. Seyf, Z. Zhou, H. Ma, Y. Zhang, Three dimensional numerical study of heat-transfer enhancement by nano-encapsulated phase change material slurry in microtube heat sinks with tangential impingement, Int. J. Heat Mass Tran. 56 (2013) 561–573.
[24] M.M.U. Rehman, Z. Qu, R. Fu, Three-dimensional numerical study of laminar confined slot jet impingement cooling using slurry of nano-encapsulated phase change material, J. Therm. Sci. 25 (2016) 431–439.
[25] M. Joseph, V. Sajith, An investigation on heat transfer performance of polystyrene encapsulated n-octadecane based nanofluid in square channel, Appl. Therm. Eng. 147 (2019) 756–769.
[26] B. Rajabifar, H.R. Seyf, Y. Zhang, S.K. Khanna, Flow and heat transfer in micro pin fin heat sinks with nano-encapsulated phase change materials, J. Heat Tran. 138 (2016).
[27] H. Reza Seyf, M.R. Wilson, Y. Zhang, H. Ma, Flow and heat transfer of nanoencapsulated phase change material slurry past a unconfined square cylinder, J. Heat Tran. (2014) 136.
[28] H. Lu, H.R. Seyf, Y. Zhang, H. Ma, Heat transfer enhancement of backward-facing step flow by using nano-encapsulated phase change material slurry, Numer. Heat Tran., Part A: Applications 67 (2015) 381–400.
[29] M. Kharati-Koopaee, A. Ghaedi, Effects of step height and particle diameter on the heat transfer and fluid flow of water-nanoencapsulated phase change material over the backward step, Int. Commun. Heat Mass Tran. 109 (2019) 104387.
[30] M. Ghalambaz, T. Groşan, I. Pop, Mixed convection boundary layer flow and heat transfer over a vertical plate embedded in a porous medium filled with a suspension of nano-encapsulated phase change materials, J. Mol. Liq. 293 (2019) 111432.
[31] M. Ghalambaz, A.J. Chamkha, D. Wen, Natural convective flow and heat transfer of nano-encapsulated phase change materials (NEPCMs) in a cavity, Int. J. Heat Mass Tran. 138 (2019) 738–749.
[32] R.Y. Emami, M. Siavashi, G.S. Moghaddam, The effect of inclination angle and hot wall configuration on Cu-water nanofluid natural convection inside a porous square cavity, Adv. Powder Technol. 29 (2018) 519–536.
[33] A. Rashad, T. Armaghani, A.J. Chamkha, M. Mansour, Entropy generation and MHD natural convection of a nanofluid in an inclined square porous cavity: effects of a heat sink and source size and location, Chin. J. Phys. 56 (2018) 193–211.
[34] N.S. Bondareva, M.A. Sheremet, H.F. Oztop, N. Abu-Hamdeh, Heatline visualization of MHD natural convection in an inclined wavy open porous cavity filled with a nanofluid with a local heater, Int. J. Heat Mass Tran. 99 (2016) 872–881.
[35] M.M. Farid, A.M. Khudhair, S.A.K. Razack, S. Al-Hallaj, A review on phase change energy storage: materials and applications, Energy Convers. Manag. 45 (2004) 1597–1615.
[36] I. Zahmatkesh, M.R.H. Shandiz, Optimum constituents for MHD heat transfer of nanofluids within porous cavities, J. Therm. Anal. Calorim. 138 (2019) 1669–1681.
[37] L. Chai, R. Shaukat, L. Wang, H.S. Wang, A review on heat transfer and hydrodynamic characteristics of nano/microencapsulated phase change slurry (N/MPCS) in mini/microchannel heat sinks, Appl. Therm. Eng. 135 (2018) 334–349.
[38] M. Ghalambaz, A. Doostani, E. Izadpanahi, A.J. Chamkha, Phase-change heat transfer in a cavity heated from below: the effect of utilizing single or hybrid nanoparticles as additives, J. Taiwan Inst. Chem. Eng. 72 (2017) 104–115.
[39] J. Buongiorno, D.C. Venerus, N. Prabhat, T. McKrell, J. Townsend, R. Christianson, Y.V. Tolmachev, P. Keblinski, L.-w. Hu, J.L. Alvarado, A benchmark study on the thermal conductivity of nanofluids, J. Appl. Phys. 106 (2009), 094312.
[40] D.C. Venerus, J. Buongiorno, R. Christianson, J. Townsend, I.C. Bang, G. Chen, S. J. Chung, M. Chyu, H. Chen, Y. Ding, Viscosity measurements on colloidal dispersions (nanofluids) for heat transfer applications, Appl. Rheol. 20 (2010) 11–17.
[41] T. Basak, S. Roy, T. Paul, I. Pop, Natural convection in a square cavity filled with a porous medium: effects of various thermal boundary conditions, Int. J. Heat Mass Tran. 49 (2006) 1430–1441.
[42] J.N. Reddy, An Introduction to the Finite Element Method, 1993. New York,.
[43] K. Kahveci, Buoyancy driven heat transfer of nanofluids in a tilted enclosure, J. Heat Tran. 132 (2010), 062501.
[44] Q. Sun, I. Pop, Free convection in a triangle cavity filled with a porous medium saturated with nanofluids with flush mounted heater on the wall, Int. J. Therm. Sci. 50 (2011) 2141–2153.
[45] M.A. Sheremet, T. Grosan, I. Pop, Free convection in a square cavity filled with a porous medium saturated by nanofluid using Tiwari and Das' nanofluid model, Transport Porous Media 106 (2015) 595–610.
[46] O. Turan, A. Sachdeva, N. Chakraborty, R.J. Poole, Laminar natural convection of power-law fluids in a square enclosure with differentially heated side walls subjected to constant temperatures, J. Non-Newtonian Fluid Mech. 166 (2011) 1049–1063.
[47] H. Cheong, Z. Siri, S. Sivasankaran, Effect of aspect ratio on natural convection in an inclined rectangular enclosure with sinusoidal boundary condition, Int. Commun. Heat Mass Tran. 45 (2013) 75–85.